HHS Public Access

Author manuscript

IEEE Trans Med Imaging. Author manuscript; available in PMC 2020 November 03.

Published in final edited form as:

IEEE Trans Med Imaging. 2020 November ; 39(11): 3278–3289. doi:10.1109/TMI.2020.2990347.

Dual Energy Differential Phase Contrast CT (DE-DPC-CT) Imaging

Xu Ji,
Department of Medical Physics, University of Wisconsin-Madison, Madison, WI 53705 USA.

Ran Zhang,
Department of Medical Physics, University of Wisconsin-Madison, Madison, WI 53705 USA.

Ke Li,
Department of Medical Physics and the Department of Radiology, University of Wisconsin-Madison, Madison, WI 53705 USA

Guang-Hong Chen
Department of Medical Physics and the Department of Radiology, University of Wisconsin-Madison, Madison, WI 53705 USA

Abstract

When more than two elemental materials are present in a given object, material quantification may not be robust and accurate when the routine two-material decomposition scheme in current dual energy CT imaging is employed. In this work, we present an innovative scheme to accomplish accurate three-material decomposition with measurements from a dual energy differential phase contrast CT (DE-DPC-CT) acquisition. A DE-DPC-CT system was constructed using a grating interferometer and a photon counting CT imaging system with two energy bins. The DE-DPC-CT system can simultaneously measure both the imaginary and the real part of the complex refractive index to enable a three-material decomposition. Physical phantom with 21 material inserts were constructed and measured using DE-DPC-CT system. Results demonstrates excellent accuracy in elemental material quantification. For example, relative root-mean-square errors of 4.5% for calcium and 5.2% for iodine have been achieved using the proposed three-material decomposition scheme. Biological tissues with iodine inserts were used to demonstrate the potential utility of the proposed spectral CT imaging method. Experimental results showed that the proposed method correctly differentiates the bony structure, iodine, and the soft tissue in the biological specimen samples. A triple spectra CT scan was also performed to benchmark the performance of the DE-DPC-CT scan. Results demonstrated that the material decomposition from the DE-DPC-CT has a much lower quantification noise than that from the triple spectra CT scan.

Keywords

phase contrast imaging; material decomposition; K-edge imaging; dual energy CT

gchen7@wisc.edu.

I. INTRODUCTION

MULTI-ENERGY x-ray computed tomography (CT), also known as spectral CT imaging, was proposed in the 1970s [1] and has been widely used in medical imaging to provide the needed elemental material differentiation and quantification when two materials demonstrate the same CT numbers under a single energy CT scan [2]–[8]. Current dual-energy CT technology has the capability to robustly decompose an unknown material into two material bases, e.g., soft tissue and bone, for material quantification purpose. However, when a third elemental material is added, e.g., a K-edge contrast agent such as iodine, the decomposition into two material bases may not be sufficient to provide the elemental material differentiation and quantification [9]. The quantification of the concentration of contrast agents, however, is closely related to several clinical tasks. For example, the quantification of iodine contrast can help to estimate the blood concentration to further differentiate tumor types [10]–[12]. It also helps the diagnosis of cardiac disease [13]–[17] and abdominal diseases [18]–[22]. The quantifications of novel contrast agents, e.g., gold, are helpful in cancer targeting [23].

Given the aforementioned clinical relevance, a three- or multi-material decomposition for quantification purposes is deemed necessary. For conventional dual energy spectral CT imaging methods, an empirical volume conservation or mass conservation hypothesis has been introduced to enable a three-material decomposition [24]–[28]. However, the accuracy of these empirical constraint-based methods depends on whether the prior knowledge is valid in a real-world scenario and these methods do not always generate robust or reliable quantification results in practice [25]. Recently, different hard-ware configurations have been introduced to utilize three different measurements to enable a robust three- or multi-material decomposition. These methods include brute force measurements using three different x-ray spectra [29], using dual-source-dual-detector systems [30], [31], using photon-counting detectors with more than two energy bins [32]–[39].

In the past decade, grating-based differential phase contrast (DPC) imaging methods including DPC-CT methods have been extensively investigated [40]–[55]. In grating-based DPC imaging, when an x-ray interferometer consisting of a set of x-ray gratings are incorporated into a conventional x-ray imaging system, the conventional x-ray CT imaging system is then upgraded into an x-ray multi-contrast system which provides conventional absorption contrast images and the additional endogenous contrast information, e.g., the phase contrast and the dark-field contrast of the image object. In CT acquisitions, the acquired DPC projection data can be reconstructed to obtain quantitative electron density of the image object. Note that one unique advantage of the DPC-CT acquisitions is that the conventional absorption contrast CT projection data can be simultaneously generated during the DPC-CT acquisition. As a result, both the DPC-CT data and the absorption CT data can be acquired in a single DPC-CT data acquisition. DPC-CT reconstruction generates an electron density image while the conventional absorption CT images display a combination of the objects' electron density and effective atomic number distribution. Therefore, the joint use of the obtained DPC-CT and absorption CT information allows us [45] and others [56] to accomplish the routine dual-energy CT objectives, without the need for dual energy spectra in the data acquisitions. In this work, we show that accurate three-material

decomposition can be accomplished using a dual-energy DPC-CT (DE-DPC-CT) acquisition. To validate the proposed scheme, an experimental DE-DPC-CT system was constructed by incorporating an x-ray grating interferometer into a photon-counting-detector based CT system with two energy bins. The theoretical foundation and experimental feasibility to perform the three-material decomposition with the DE-DPC-CT system was investigated.

II. METHODS AND MATERIALS

A. Three-material decomposition in spectral CT with three energy spectra

In diagnostic x-ray energy range (10 keV - 140 keV), if a K-edge material (e.g., iodine) is presented in an image object, the x-ray linear attenuation coefficient of a material can be decomposed into three bases [9]:

$$\mu(E) = \mu_{\mathrm{cs}}(E) + \mu_{\mathrm{PE}}(E) + \mu_{\mathrm{PE,K}}(E), \tag{1}$$

where μ is energy dependent linear attenuation coefficients of the three physical bases [Compton scattering (CS), photoelectric effect (PE) without the K-edge effect, and the K-edge photoelectric effect]. Alternatively, the attenuation coefficient can also be decomposed into three material bases, such as water, calcium and the K-edge material [57]:

$$\begin{aligned}\mu(E) &= a_{\mathrm{water}}\mu_{\mathrm{water}}(E) + a_{\mathrm{Ca}}\mu_{\mathrm{Ca}}(E) + a_{\mathrm{K}}\mu_{\mathrm{K}}(E) \\ &= \sum_{i=1}^{3} a_i\mu_i(E),\end{aligned} \tag{2}$$

where a_i represents the decomposition coefficients and the indices $i = 1, 2, 3$ represent water, calcium, and the K-edge material, respectively. In order to determine the three decomposition coefficients for material quantification purposes, a minimum of three measurements at three different spectra are required. The information provided by dual-energy systems alone without any prior knowledge is not sufficient to solve the three unknowns for a three-material decomposition.

B. Three-material decomposition in DE-DPC-CT

When a grating interferometer is introduced to a system, additional information regarding the refractive index of the material can be extracted. Assuming that the refractive index is written as $n = 1 - \delta + i\beta$; here δ is related to the electron density as [45]

$$\delta(E) = \rho_e \times \frac{r_0\hbar^2c^2}{2\pi E^2}, \tag{3}$$

where $r_0 = 2.82 \times 10^{-15}$ m is the classical radius of the electron, $\hbar$ is the reduced Planck constant and c is the speed of light. Meanwhile, it can be derived that for a material decomposed into three basis materials as shown in (2), its electron density is related to the electron density of each basis material as

$$\rho_e = \sum_{i=1}^{3} a_i \rho_{e,i}, \tag{4}$$

where a_i are the same decomposition coefficients as those in (2). Details of this derivation are shown in the appendix. The δ component of the complex refractive index can be further written as follows:

$$\delta(E) = \rho_e \times \frac{r_0 \hbar^2 c^2}{2\pi E^2} = \sum_{i=1}^{3} a_i \delta_i(E), \tag{5}$$

where $\delta_i(E) = \rho_{e,i} \times \frac{r_0 \hbar^2 c^2}{2\pi E^2}$.

By comparing (2) and (5), one can observe that both the linear attenuation coefficient $\mu(E)$ and the real part of the refractive index, $\delta(E)$, can be decomposed into three material bases with the same decomposition coefficients a_i ($i = 1, 2, 3$). This observation leads to the proposed three-material decomposition method in this paper.

The proposed material decomposition method is performed in the reconstructed image domain. Assuming that the three calibration materials with attenuation coefficients [$\mu_1(E)$, $\mu_2(E)$, $\mu_3(E)$] and electron densities ($\rho_{e,1}$, $\rho_{e,2}$, $\rho_{e,3}$) are known *a priori*. The decomposition of the attenuation coefficient of an unknown material can be written in a mathematical form

$$\mu(E) = a_1 \mu_1(E) + a_2 \mu_2(E) + a_3 \mu_3(E)\,. \tag{6}$$

For a phase contrast CT system that is equipped with a photon counting detector with two energy bins, the following three equations can be established from data collected in a single CT acquisition:

$$\mu_L = a_1 \mu_{1,L} + a_2 \mu_{2,L} + a_3 \mu_{3,L}; \tag{7}$$

$$\mu_H = a_1 \mu_{2,H} + a_2 \mu_{2,H} + a_3 \mu_{3,H}; \tag{8}$$

$$\rho_e = a_1 \rho_{e,1} + a_2 \rho_{e,2} + a_3 \rho_{e,3}, \tag{9}$$

where $\mu_{i,L/H}$ represents the attenuation coefficients of the i–th basis measured from the low energy or high energy bin, respectively. Since the relationship between δ and x-ray energy E solely relies on the $1/E^2$ term as shown in (3), equation (9) is equivalent to

$$\delta = a_1 \delta_1 + a_2 \delta_2 + a_3 \delta_3, \tag{10}$$

where δ is measured from either the low or high energy beam.

Finally the equations can be summarized in the following matrix form

$$M\begin{bmatrix} a_1 \\ a_2 \\ a_3 \end{bmatrix} = \begin{bmatrix} \mu_L \\ \mu_H \\ \delta \end{bmatrix}, \tag{11}$$

where the 3 × 3 matrix M is defined as follows:

$$M = \begin{bmatrix} \mu_{1,L} & \mu_{2,L} & \mu_{3,L} \\ \mu_{1,H} & \mu_{2,H} & \mu_{3,H} \\ \delta_1 & \delta_2 & \delta_3 \end{bmatrix} \tag{12}$$

Since the matrix M is full rank, the three decomposition coefficients a_i can be easily obtained by inverting the matrix as follows:

$$\begin{bmatrix} a_1 \\ a_2 \\ a_3 \end{bmatrix} = M^{-1}\begin{bmatrix} \mu_L \\ \mu_H \\ \delta \end{bmatrix}, \tag{13}$$

where M^{-1} is the inverse of the matrix M. As dictated by the above equation, as long as the dual energy DPC-CT acquisition is performed, the reconstructed images μ_H, μ_L, and δ can be used as inputs to generate the desired three-material decomposition coefficients a_1, a_2, and a_3.

In practice, the matrix M is constructed from measurements of the attenuation coefficients and phase signals of the three materials acquired from a DE-DPC-CT scan. Following that, further measurements of μ_L, μ_H, δ corresponding to an unknown material are plugged into (13) as inputs to determine the corresponding a_i values (i = 1, 2, 3).

C. Experimental methods

To validate the proposed three-material decomposition via a DE-DPC-CT acquisition, physical experiments were performed on a benchtop DPC-CT system with a photon counting detector (Fig. 1).

1) DE-DPC-CT data acquisition system: The system uses a medical grade rotating-anode x-ray tube with 0.5 mm nominal focal spots (model G1582, Varian Medical Systems, Inc., Salt Lake City, UT) and a CdTe-based photon counting detector (model XC-Thor, XCounter AB, Sweden). The detector has a pixel array of 1024 × 512 array of 100 μm and two adjustable energy thresholds. The grating interferometer consists of a source grating G0, a phase grating G1, and an analyzer grating G2. The G1 grating is designed for 28 keV x-rays. The parameters of the gratings are shown in Table I. The distance between G0 and G1 was set to 150 cm, and the distance between G1 and G2 was 17.5 cm. The image object was placed between G0 and G1. The distance from the x-ray source to the isocenter is 179 cm and that from the x-ray source to the detector is 231 cm.

2) Experimental phantoms and biological specimens used in validation studies: In order to validate and evaluate the proposed method, an in-house physical phantom with different material mixtures ($CaCl_2$ and iodine) and concentrations were fabricated. All the materials were dissolved in water. The concentrations of $CaCl_2$ solutions are 20, 25, 40, 50, 60, 75, 80, and 100 mg/mL; the concentrations of iodine solutions are 2, 2.5, 4, 5, 6, 7.5, 8, and 10 mg/mL. Mixtures of $CaCl_2$ and iodine solutions were also made. The concentrations are 25 mg/mL $CaCl_2$ with 7.5 mg/mL iodine, 50 mg/mL $CaCl_2$ with 5 mg/mL iodine, and 75 mg/mL $CaCl_2$ with 2.5 mg/mL iodine. As shown in Fig. 2 (a), the solutions were sealed in plastic straws and the straws were then placed in a water-filled cylindrical PMMA container for the CT scan. The diameters of the straws and the PMMA container are 6 mm and 25 mm, respectively. The inserts also include a thin, solid PMMA cylinder with a diameter of 5.5 mm. The inserts were grouped into three groups and three CT scans with the same setup were performed.

In addition to the physical phantom, biological specimens were also included as part of the experiment, as shown in Fig. 2 (b). Chicken wings which have been Formalin-fixed were kept in a hollow cylindrical PMMA tube as the image object. To add a third material to the phantom, a vial of iodine solution with a concentration of 32 mg/mL was also kept in the PMMA tube during the scan.

3) Data acquisition parameters: For the phase contrast CT scan, the tube potential was set at 50 kVp with a mean energy of 32 keV. The fringe visibility of the system was approximately 0.13 under this x-ray spectrum. The two energy thresholds of the photon counting detector were set at 15 keV and 35 keV to perform the dual energy acquisition. The energy threshold is empirically optimized by requiring that the post-object photon numbers in the low energy bin (15–35 keV) and the high energy bin (35–50 keV) are approximately equal. In our experimental studies, the anti-coincidence function of the detector was turned on. The projection data were acquired at 360 view angles. For each view angle, a phase stepping procedure was performed with five phase steps. The tube current was set to be 10 mA and the exposure time for each phase setup is 0.5 s, resulting in a 25 mAs exposure for each phase stepping procedure.

The phase retrieval process was performed from the phase stepping data and images were reconstructed using the standard filtered back-projection method (low-pass cosine kernel for absorption CT and Hilbert kernel for phase CT). The reconstructed image has a pixel matrix of 512 × 512, a field of view of 30 mm and a slice thickness of 1.5 mm. For the decomposition, the 100 mg/mL $CaCl_2$, the 10 mg/mL iodine and water were chosen as the material bases. By measuring the attenuation coefficients and the phase signal for the three basis materials from the reconstructed images, the decomposition matrix M in (11) was determined and the material decomposition was performed.

D. Triple spectra scan as a comparison

To benchmark the performance of the DE-DPC-CT system, a triple spectra scan was performed using the same benchtop system. Imaging parameters between the DE-DPC-CT scan and the triple spectra scan were the same, e.g., the tube potential, the tube current and

the exposure time. Since the two post-object gratings (the phase grating and the analyzer grating) were not needed for a conventional CT scan and decrease the dose efficiency by attenuating post-object photons, these two gratings were removed for the triple spectra scan. However, the pre-object grating was still used in the triple spectra scan in order to match the pre-object energy spectra and the dose delivered to the image object to those of the DE-DPC-CT. The detector thresholds were set at 15 keV, 27 keV and 38 keV to ensure the post-object photon numbers in the three energy bins (15–27 keV, 27–38 keV, 38–50 keV) are approximately the same. Although the photon counting detector used in this study has only two adjustable thresholds, the triple spectra scan can be achieved by scanning the image object twice. The first scan was performed with the thresholds setting at 15 keV and 27 keV; then the 15–27 keV energy bin can be acquired. The second scan was performed with the thresholds set at 27 keV and 38 keV so the 27–38 keV and the 38–50 keV energy bins can be acquired. This is equivalent to scanning the image object using a photon counting detector with three energy thresholds. After the measurement of the attenuation coefficients of the three calibration materials in the three energy bins, an image domain decomposition was performed [58]. The same in-house phantoms were scanned for performance comparisons.

III. RESULTS

A. Reconstructed images from DE-DPC-CT

In order to differentiate the different inserts, the inserts were indexed and the corresponding materials and concentrations are listed in Table II. The inserts were divided into three groups and inserts indices for each group are shown in Fig. 3(a), 4(a), and 5(a), respectively.

The reconstructed absorption and phase CT images for the inserts are shown in Fig. 3–5(b)–(d). In these presented images, the low energy bin corresponds to 15–35 keV, the high energy bin corresponds to 35–50 keV and the full energy bin corresponds to 15–50 keV.

B. Three-material decomposition from DE-DPC-CT

As mentioned in the previous section, the 100 mg/mL $CaCl_2$ (#2), the 10 mg/mL iodine (#10) and water (#1) were chosen as the three basis materials. To accomplish the desired three-material decomposition, the measured linear attenuation coefficients corresponding to the low and high energy bin and the δ values corresponding to the full energy bin were used to construct the decomposition matrix M as follows:

$$M = \begin{bmatrix} 0.334 & 0.546 & 0.478 \\ 0.255 & 0.374 & 0.448 \\ 0.226 \times 10^{-6} & 0.237 \times 10^{-6} & 0.233 \times 10^{-6} \end{bmatrix}$$

The first two rows of M have a unit of [cm^{-1}].

Using the above matrix M, the three-material decomposition was performed following (13). Results are presented in Fig. 3–5 (e)–(h). Given the decomposition results, some qualitative analysis can be performed. For inserts #14 (5 mg/mL iodine) in Fig. 3, since it contains no calcium, it should appear dark in the corresponding calcium map, which is consistent with

Fig. 3 (e). Meanwhile, insert #21 (PMMA) in Fig. 4 does not contain iodine, and it appears dark in the corresponding iodine map (Fig. 4 (f)).

C. Quantification accuracy of the three-material decomposition

Quantitative measurements of the decomposition coefficients were performed and the results are summarized in Table III. The measured coefficients were converted to the material concentrations. The measured concentrations were then compared with the ground truth values and the comparison was shown in Fig. 6 (a) and (c). A linear fit was performed for the measured values and ground truth values. The coefficients of the linear fit and the coefficients of determination are shown in the plot. The differences between the measured and the ground truth concentrations are shown in Fig. 6 (b) and (d). The root-mean-square errors (RMSE) of the measured concentrations in comparison to the ground truths are 1:4 ± 0:90 mg/mL for $CaCl_2$ and 0:20±0:094 mg/mL for iodine. The relative RMSE is 4:5% ± 3:5% for CaCl2 and 5:2% ± 3:1% for iodine.

D. Three-material decomposition applied to biological specimens

The reconstructed absorption and phase CT images for the chicken wing are shown in Fig. 7(a)–(c). As one can tell, the iodine solution has similar linear attenuation coefficient with the bones (Fig. 7 (a)–(b)), but has a much lower electron density (smaller δ value, as shown in Fig. 7 (c)). Therefore, the phase image indeed provided the needed extra information to perform a three-material differentiation and decomposition. The material decomposition was then performed and the coefficients of decomposition matrix M are the same with that in Sec. (III-A). The decomposition results are shown in Fig. 7 (d)–(f). The proposed decomposition method correctly differentiated the bones and the iodine solution.

E. Comparison with results from the triple spectra scan

An example of the reconstructed absorption CT images for the inserts corresponding to the three energy bins are shown in Fig. 8 (b)–(d). In these presented images, the low energy bin corresponds to 15–27 keV, the middle energy bin corresponds to 27–38 keV and the high energy bin corresponds to 38–50 keV. The decomposed material basis maps are shown in Fig. 8 (e)–(f) and Fig. 9–10 (b)–(d). Quantitative measurements of the decomposition coefficients are performed and the results were summarized in Table IV. The measured coefficients were converted to the material concentration. In comparison to the ground truth concentrations, the root mean square errors (RMSE) of the measured concentrations are 1.5 ± 1.1 mg/mL for $CaCl_2$ and 0.24 ± 0.14 mg/mL for iodine. The relative RMSE is 5.0% ±3.9% for $CaCl_2$ and 5.0%±2.8% for iodine.

IV. DISCUSSION

In this work, a new three-material decomposition method was developed using a DE-DPC-CT acquisition technique. Theoretical analysis showed that the decomposition of the electron density shares the same decomposition coefficients with those of the linear attenuation coefficients, which provided the theoretical foundation for the proposed method. Physical experiments were performed for the purpose of validation. Quantification phantoms used in the experiments included the $CaCl_2$ and iodine solutions with different

concentrations. The quantification accuracy evaluated by the RMSE is 1.4 mg/mL for $CaCl_2$ and 0.20 mg/mL for iodine. Biological samples with iodine inserts were also scanned to test the material differentiation capability of the proposed method for real biological tissue. The proposed method correctly differentiated the bone in the chicken wing and the iodine insert.

It should be noted that the dark-field image could potentially be used for material decomposition since it has certain energy dependence [59], [60]. If this is a viable choice, the three-material decomposition may be achieved from three different contrast mechanisms without the need of a dual energy scan, which would be an direct extension of the method developed in Ref. [45]. However, it is well known that dark-field contrast strongly depends on the shape and the orientation of the image object [61], [62]. Therefore, the feasibility to incorporate the dark-field images in three-material decomposition remains an open question. As a result, the dark field contrast was not used for three-material decomposition in this study.

To benchmark the quantification accuracy of the proposed three-material decomposition, a triple-spectra scan was performed using the same benchtop system. The quantification biases were 1.5 mg/mL for $CaCl_2$ and 0.24 mg/mL for iodine. Such quantification biases were a little bit higher than those from the DE-DPC-CT scan, although we admitted that there was no significant difference. The noise levels of decomposed images from the triple spectra scan, however, were much higher than those from DE-DPC-CT, as shown in the qualitative comparison between decomposed basis maps (e.g., Fig. 3 and Fig. 8 (e)–(g)) or in the quantitative comparison between Table III and Table IV. These results indicate that the proposed DE-DPC-CT-based three-material decomposition method may have potential advantages over the conventional absorption CT scan with triple spectra: (i) The noise power spectrum of the DPC-CT images has a greater low-frequency component, which is different from the absorption CT images [63], [64]. This peculiar noise property in DPC-CT may help to reduce the noise variance, especially for reconstructed images with a small pixel size [46]. (ii) The improved material decomposition performance may be attributed to the use of two different contrast mechanisms for the DE-DPC-CT. In traditional spectral CT imaging, only the x-ray absorption contrast mechanism is utilized, and thus the material decomposition performance strongly depends on how well the three energy spectra are separated. As shown in earlier studies [1], [24], [65], a strong spectral overlap in conventional dual-energy or multi-energy CT can lead to a degradation in the precision and accuracy of the material decomposition results. In contrast, the proposed method leverages the mutually complementary information provided by the absorption contrast and phase contrast images to accomplish material decomposition, which reduces the dependence on spectral separation.

It is important to understand that the quantification errors of the proposed DE-DPC-CT method may depend on the following confounding factors: (i) The theoretical modeling of the linear attenuation coefficient includes the Compton scattering and the photoelectric effect but neglected the coherent scattering process. According to the database provided by the NIST XCOM website [66], for a 30 keV photon interacting with calcium, the coherent scattering contributed to about 5% of the total interaction cross-section. The neglection of the coherent scattering processes in data analysis may contribute to the quantification error in our experimental results. The impact of coherent scattering on the quantification accuracy

of the proposed three-material decomposition scheme remains to be further studied. (ii) Another potential error source is the signal bias in DPC imaging. Due to the cyclic nature of the phase contrast signal, the phase wrapping effect may lead to signal bias, especially when the differential phase signal is close to $\pm\pi$ for systems with relatively high sensitivity, as shown in our previous work [67]. This intrinsic statistical bias is more evident at the boundaries between two materials since there is a relatively large phase difference and the DPC signal is high. The statistical signal bias in the measured projection data will propagate through the entire imaging chain, resulting in artifacts in the reconstructed DPC-CT images. The artifacts can be seen in Fig. 7 (c), as the boundaries between the chicken wing and air appears darker than the interior tissue. The bias also contributes to the noise streaks around the air bubbles in Fig. 4 (d). This will lead to further quantification inaccuracies as the boundaries between the image object and air will have erroneous $CaCl_2$ or iodine compositions (e.g., Fig. 5 (e)–(f)). (iii) The beam hardening effect may be another source of error. Since the decomposition is performed in the image domain, a small object with negligible beam hardening artifacts is assumed. When this assumption is severely violated, the beam hardening image artifacts may propagate to the final decomposition and lead to inaccurate decomposition results. In this case beam hardening correction methods should be performed before or after the reconstruction [68]. Although beam hardening is not evident in this study, the impact of beam hardening effect on three-material decomposition accuracy should be carefully investigated when the large or highly attenuating image objects are concerned.

One limitation of the studies presented in this paper is that the experiments were performed at a tube potential of 50 kVp, which is significantly lower than the typical tube potential used for clinical dual-energy or multi-energy CT scans. The selection of the tube potential in this work is limited by the x-ray grating interferometer, which was originally designed for an x-ray beam with a mean energy of 28 keV. When grating interferometer can be fabricated to work at higher x-ray energies [69]–[72], this limitation of our work can be better overcome. However, at higher operation energies, the performance of the proposed three-material decomposition method will need to be carefully investigated. Note that the performance of the three-material decomposition method proposed in this work relies on the complementary information provided by the DPC mechanism. First of all, when x-ray energy is elevated to the higher end, the DPC-CT signal significantly decreases because it is inversely proportional to the square of the x-ray energy. This may decrease the signal-to-noise ratio of the DPC-CT images and further degrade the decomposition results. Additionally, the relative contribution of Compton scattering effect to the absorption contrast increases as the energy increases. For materials with relatively low atomic numbers, the Compton scattering dominates the attenuation cross-section at higher energies (> 70 keV). In this case, since the Compton scattering cross-section and the DPC signal are both proportional to the electron density, the attenuation and the DPC signal becomes less complementary and material decomposition may be a challenge [69]. However, for materials with relatively high atomic numbers, e.g., contrast agents, the photoelectric cross-section still contributes considerable amount to the total attenuation at higher energies. Overall, it is likely that there will be a transitional energy range that the performance of the proposed DE-DPC-CT method might

be inferior to other methods such as triple spectra CT scans. However, the final outcome remains to be explored in future with an interferometer operated at higher energies.

We also acknowledge some other limitations in our studies. As stated before, the spectrum selected to perform experimental studies was determined by the grating design and whether such selection leads to an optimal material decomposition remains unknown. Actually, the selection of tube potential has a significant impact on the decomposition. On one hand, increasing the tube potential may decrease the fringe visibility in DPC-CT imaging. As a result, noise may increase and thus image quality in DPC-CT images drops [46], [73], [74]. This result is due to the fact that x-ray interferometer is energy sensitive; the x-ray gratings are often designed to work at an optimal energy and a deviation from the optimal operation energy of the interferometer results in the degradation in fringe visibility and the DPC-CT image quality. On the other hand, an increase of the tube potential may allow a better spectral separation in dual energy CT scans and thus a better noise property in dual energy CT images. Therefore, it is expected that there should be some optimal x-ray spectra for the proposed DE-DPC-CT-based three-material decomposition, which warrant more detailed future studies. Moreover, the x-ray filtration also plays an important role in the optimization of x-ray spectrum. As shown in recent works, when novel x-ray beam filters, e.g., the iodine filter, is used, x-ray spectra can be optimized for photon counting CT to perform optimal material decomposition [57]. Therefore, it is anticipated that the x-ray spectrum shape could also be optimized in the proposed three-material decomposition method for an improved result. The selection of the energy thresholds of the detector was empirically optimized to equally allocate the post-object photons in each energy bin. In this case, the noise levels of the reconstructed absorption images from each energy bin were similar to each other. However, it remains to be investigated whether some other optimization criteria should be used such that the quantification accuracy is maximally achieved for the proposed three-material decomposition method [75], [76]. Finally, in this work, we only used the most basic data processing procedures, including a conventional filtered-back projection reconstruction method and an image-domain decomposition method to process data. However, previous studies have shown that statistical reconstruction method may help to decrease the signal bias in DPC-CT [77] and improve material quantification accuracy [78]–[83]. Therefore, the impact of these more advanced image processing tools on the proposed DE-DPC-CT-based three-material decomposition scheme should also be further investigated as future work.

V. CONCLUSION

A DE-DPC-CT imaging method was developed to perform accurate three-material decomposition. Such an imaging method is able to simultaneously produce both the x-ray dual energy absorption information and the x-ray DPC information. Experimental results demonstrated that a joint use of the measured dual energy absorption CT information and DPC-CT information enables accurate three-material decomposition. The results also demonstrated potential advantages of the proposed DE-DPC-CT imaging method over the conventional triple spectra CT method in three-material decomposition.

ACKNOWLEDGMENT

The authors would like to thank Mang Feng for providing the GPU-based CT reconstruction code, Dan Bushe for the editorial assistance, and the anonymous reviewers for their comments and suggestions to improve the quality of this paper.

This work was partially supported by the National Institute of Biomedical Imaging and Bioengineering of the National Institutes of Health under Award Number R01EB020521, and by the Office of the Assistant Secretary of Defense for Health Affairs, through the Breast Cancer Research Program, under Award No. W81XWH-16-1-0031.

APPENDIX I

PROOF THE DECOMPOSITION COEFFICIENTS OF THE ELECTRON DENSITY

As shown in (1), when the K-edge of a specific element is taken into consideration, the linear attenuation of a compound material can be decomposed into three bases

$$\mu(E) = \mu_{\mathrm{cs}}(E) + \mu_{\mathrm{PE}}(E) + \mu_{\mathrm{PE,K}}(E)\,. \tag{14}$$

The contribution from the Compton scattering process can be written as

$$\mu_{\mathrm{CS}} = \rho\frac{N_A}{A}Z\sigma_{\mathrm{KN}}(E), \tag{15}$$

where ρ, N_A, A, Z and σ_{KN} are the mass density, Avogadro's number, atomic mass, effective atomic number and the Klein-Nishina cross-section, respectively. Since the electron density $\rho_e = \frac{Z\rho N_A}{A}$, then

$$\mu_{\mathrm{CS}} = \rho_e\sigma_{\mathrm{KN}}(E)\,. \tag{16}$$

For the photoelectric effect without the K-edge in diagnostic range, the dependence of the linear attenuation coefficient on energy can be approximated as

$$\mu_{\mathrm{PE}}(E) = \frac{\xi}{E^3}, \tag{17}$$

where ξ is a coefficient with no dependence on energy E. ξ is related to the properties of the material, e.g., density, effective atomic number, atomic mass, etc. For K-edge photoelectric effect corresponding to a specific K-edge element, the dependence of the linear attenuation coefficients on the x-ray energy is given as

$$\mu_{\mathrm{PE,K}}(E) = \eta\sigma_{\mathrm{PE,K}}(E), \tag{18}$$

where η is a coefficient with no dependence on energy but is related to the concentration of the K-edge element in the compound material. $\sigma_{\mathrm{PE,K}}$ is the energy-dependent cross-section of the photoelectric effect with K-edge. Given the above equations, equation (1) can be written as

$$\mu(E) = \rho_e \sigma_{\mathrm{KN}}(E) + \frac{\xi}{E^3} + \eta \sigma_{\mathrm{PE,K}}(E)\,. \tag{19}$$

As shown in (2), a compound material can also be decomposed into three material bases

$$\mu(E) = \sum_{i=1}^{3} a_i \mu_i(E)\,. \tag{20}$$

For each basis, following the previous analysis, its linear attenuation coefficient can be written as

$$\mu_i(E) = \rho_{e,i} \sigma_{\mathrm{KN}}(E) + \frac{\xi_i}{E^3} + \eta_i \sigma_{\mathrm{PE,K}}(E)\,. \tag{21}$$

By replacing the μ_i items in (20) with the expression in (21), (20) can be further written as

$$\begin{aligned} \mu(E) &= \sum_{i=1}^{3} a_i \left[\rho_{e,i} \sigma_{\mathrm{KN}}(E) + \frac{\xi_i}{E^3} + \eta_i \sigma_{\mathrm{PE,K}}(E) \right] \\ &= \left(\sum_{i=1}^{3} a_i \rho_{e,i} \right) \sigma_{\mathrm{KN}}(E) + \frac{\left(\sum_{i=1}^{3} a_i \xi_i \right)}{E^3} \\ &+ \left(\sum_{i=1}^{3} a_i \eta_i \right) \sigma_{\mathrm{PE,K}}(E)\,. \end{aligned} \tag{22}$$

Since both (19) and (22) give the expression of $\mu(E)$, the right-hand sides of the two equations must be equal:

$$\rho_e \sigma_{\mathrm{KN}}(E) + \frac{\xi}{E^3} + \eta \sigma_{\mathrm{PE,K}}(E) \tag{23}$$

$$\begin{aligned} &= \left(\sum_{i=1}^{3} a_i \rho_{e,i} \right) \sigma_{\mathrm{KN}}(E) + \frac{\left(\sum_{i=1}^{3} a_i \xi_i \right)}{E^3} \\ &+ \left(\sum_{i=1}^{3} a_i \eta_i \right) \sigma_{\mathrm{PE,K}}(E)\,. \end{aligned} \tag{24}$$

This equation is valid for any E. Since the bases $\sigma_{\mathrm{KN}}(E)$, $1/E^3$ and $\sigma_{\mathrm{PE,K}}(E)$ are linearly independent, the corresponding coefficients must be equal, which means that

$$\rho_e = \sum_{i=1}^{3} a_i \rho_{e,i}\,. \tag{25}$$

This is (4) in the main text, which dictates that the decomposition coefficients of electron density and linear attenuation are same when the used material bases are the same.

REFERENCES

[1]. Alvarez R and Macovski A, "Energy-selective reconstructions in x-ray computerised tomography," Phys. Med. Biol, vol. 21, pp. 733–744, 1976. [PubMed: 967922]

[2]. Kalender WA, Perman WH, Vetter JR, and Klotz E, "Evaluation of a prototype dual-energy computed tomographic apparatus. i. phantom studies," Med. Phys, vol. 13, no. 3, pp. 334–339, 1986. [PubMed: 3724693]

[3]. Ergun DL, Mistretta CA, Brown DE, Bystrianyk RT, Sze WK, Kelcz F et al., "Single-exposure dual-energy computed radiography: improved detection and processing." Radiology, vol. 174, no. 1, pp. 243–249, 1990, pMID: 2294555. [PubMed: 2294555]

[4]. Flohr TG, McCollough CH, Bruder H, Petersilka M, Gruber K, Süss C et al., "First performance evaluation of a dual-source CT (DSCT) system," Eur. Radiol, vol. 16, no. 2, pp. 256–268, 2 2006. [PubMed: 16341833]

[5]. Zimmerman KC, Sidky EY, and Schmidt TG, "Experimental study of two material decomposition methods using multi-bin photon counting detectors," in Medical Imaging 2014: Physics of Medical Imaging, vol. 9033 SPIE, 2014, pp. 989–994.

[6]. McCollough CH, Leng S, Yu L, and Fletcher JG, "Dual- and Multi-Energy CT: Principles, Technical Approaches, and Clinical Applications," Radiology, vol. 276, no. 3, pp. 637–653, 2015, pMID: 26302388. [PubMed: 26302388]

[7]. Atak H and Shikhaliev PM, "Dual energy CT with photon counting and dual source systems: comparative evaluation," Phys. Med. Biol, vol. 60, no. 23, p. 8949, 2015. [PubMed: 26539971]

[8]. Leng S, Zhou W, Yu Z, Halaweish A, Krauss B, Schmidt B et al., "Spectral performance of a whole-body research photon counting detector CT: quantitative accuracy in derived image sets," Phys. Med. Biol, vol. 62, no. 17, pp. 7216–7232, 8 2017. [PubMed: 28726669]

[9]. Roessl E and Proksa R, "K-edge imaging in x-ray computed tomography using multi-bin photon counting detectors," Phys. Med. Biol, vol. 52, no. 15, pp. 4679–4696, 7 2007. [PubMed: 17634657]

[10]. Lee SH, Hur J, Kim YJ, Lee H-J, and Hong YJ, "Additional value of dual-energy CT to differentiate between benign and malignant mediastinal tumors : An initial experience," Eur. J. Radiol, vol. 82, no. 11, pp. 2043–2049, 2013. [PubMed: 23820175]

[11]. Mileto A, Marin D, Alfaro-Cordoba M, Ramirez-Giraldo JC, Eusemann CD, Scribano E et al., "Iodine Quantification to Distinguish Clear Cell from Papillary Renal Cell Carcinoma at Dual-Energy Multidetector CT: A Multireader Diagnostic Performance Study," Radiology, vol. 273, no. 3, pp. 813–820, 2014, pMID: 25162309. [PubMed: 25162309]

[12]. Kaltenbach B, Wichmann JL, Pfeifer S, Albrecht MH, Booz C, Lenga L et al., "Iodine quantification to distinguish hepatic neuroendocrine tumor metastasis from hepatocellular carcinoma at dual-source dual-energy liver CT," Eur. J. Radiol, vol. 105, no. May, pp. 20–24, 2018. [PubMed: 30017280]

[13]. Chevance V, Damy T, Tacher V, Legou F, Ridouani F, Luciani A et al., "Myocardial iodine concentration measurement using dual-energy computed tomography for the diagnosis of cardiac amyloidosis: a pilot study," Eur. Radiol, vol. 28, no. 2, pp. 816–823, 2018. [PubMed: 28812126]

[14]. Assen MV, Lavra F, Schoepf UJ, Jacobs BE, Williams BT, Thompson ZM et al., "Iodine quantification based on rest/stress perfusion dual energy CT to differentiate ischemic, infarcted and normal myocardium," Eur. J. Radiol, vol. 112, no. January, pp. 136–143, 2019. [PubMed: 30777202]

[15]. Poulter R, Wood DA, Starovoytov A, Smith S, Chitsaz M, and Mayo J, "Quantified dual energy computed tomography perfusion imaging using myocardial iodine concentration: Validation using CT derived myocardial blood flow and invasive fractional flow reserve in a porcine model," J. Cardiovasc. Comput. Tomogr, vol. 13, no. 2, pp. 86–91, 2019. [PubMed: 30718182]

[16]. Scherer K, Hammel J, Sellerer T, Mechlem K, Renger B, Bahr A et al., "Dynamic quantitative iodine mocardial perfusion imaging with dual-layer CT using a porcine model," Sci. Rep, vol. 9, no. 1, p. 16046, 2019. [PubMed: 31690759]

[17]. Ohta Y, Kishimoto J, Kitao S, Yunaga H, Mukai-Yatagai N, Fujii S et al., "Investigation of myocardial extracellular volume fraction in heart failure patients using iodine map with rapid-kv switching dual-energy CT: Segmental comparison with MRI T1 mapping," J. Cardiovasc. Comput. Tomogr, 2019.

[18]. Fulwadhva UP, Wortman JR, and Sodickson AD, "Use of dual-energy CT and iodine maps in evaluation of bowel disease," Radio-Graphics, vol. 36, no. 2, pp. 393–406, 2016, pMID: 26963452.

[19]. Agrawal MD, Oliveira GR, Kalva SP, Pinho DF, Arellano RS, and Sahani DV, "Prospective comparison of reduced-iodine-dose virtual monochromatic imaging dataset from dual-energy CT angiography with standard-iodine-dose single-energy CT angiography for abdominal aortic aneurysm," Am. J. of Roentgenol, vol. 207, no. 6, pp. W125–W132, 9 2016. [PubMed: 27610820]

[20]. Martin SS, Czwikla R, Wichmann JL, Albrecht MH, Lenga L, Savage RH et al., "Dual-energy CT-based iodine quantification to differentiate abdominal malignant lymphoma from lymph node metastasis," Eur. J. Radiol, vol. 105, pp. 255–260, 2018. [PubMed: 30017291]

[21]. Kaltenbach B, Wichmann JL, Pfeifer S, Albrecht MH, Booz C, Lenga L et al., "Iodine quantification to distinguish hepatic neuroendocrine tumor metastasis from hepatocellular carcinoma at dual-source dual-energy liver CT," Eur. J. Radiol, vol. 105, pp. 20–24, 2018. [PubMed: 30017280]

[22]. Kawamoto S, Fuld MK, Laheru D, Huang P, and Fishman EK, "Assessment of iodine uptake by pancreatic cancer following chemotherapy using dual-energy CT," Abdominal Radiology, vol. 43, no. 2, pp. 445–456, 2018. [PubMed: 29473093]

[23]. Mahan MM and Doiron AL, "Gold Nanoparticles as X-Ray, CT, and Multimodal Imaging Contrast Agents : Formulation, Targeting, and Methodology," J. Nanomater, 2018.

[24]. Kelcz F, Joseph PM, and Hilal SK, "Noise considerations in dual energy CT scanning," Med. Phys, vol. 6, no. 5, pp. 418–425, 1979. [PubMed: 492076]

[25]. Liu X, Yu L, Primak AN, and McCollough CH, "Quantitative imaging of element composition and mass fraction using dual-energy CT: Three-material decomposition," Med. Phys, vol. 36, no. 5, pp. 1602–1609, 2009. [PubMed: 19544776]

[26]. Malusek A, Karlsson M, Magnusson M, and Carlsson GA, "The potential of dual-energy computed tomography for quantitative decomposition of soft tissues to water, protein and lipid in brachytherapy," Phys. Med. Biol, vol. 58, no. 4, pp. 771–785, 1 2013. [PubMed: 23322084]

[27]. Mendonca PRS, Lamb P, and Sahani DV, "A Flexible Method for Multi-Material Decomposition of Dual-Energy CT Images," IEEE Trans. Med. Imag, vol. 33, no. 1, pp. 99–116, 1 2014.

[28]. Li Z, Leng S, Yu L, Yu Z, and McCollough CH, "Image-based material decomposition with a general volume constraint for photon-counting CT," in Medical Imaging 2015: Physics of Medical Imaging, vol. 9412 SPIE, 2015, pp. 190–197.

[29]. Kim D, Lee S, and Jeon P-H, "Experimental results of use of triple-energy x-ray beam with k-edge filter in multi-energy imaging," J. Instrum, vol. 11, no. 04, pp. P04 009–P04 009, 4 2016.

[30]. Yu L, Ren L, Li Z, Leng S, and McCollough CH, "Dual-source multienergy CT with triple or quadruple x-ray beams," J. Med. Imaging, vol. 5, no. 3, pp. 1–9, 2018.

[31]. Ren L, McCollough CH, and Yu L, "Three-material decomposition in multi-energy CT: impact of prior information on noise and bias," in Medical Imaging 2018: Physics of Medical Imaging, vol. 10573 SPIE, 2018, pp. 363–368.

[32]. Schlomka JP, Roessl E, Dorscheid R, Dill S, Martens G, Istel T et al., "Experimental feasibility of multi-energy photon-counting K-edge imaging in pre-clinical computed tomography," Phys. Med. Biol, vol. 53, no. 15, p. 4031, 2008. [PubMed: 18612175]

[33]. Shikhaliev PM, "Energy-resolved computed tomography: first experimental results," Phys. Med. Biol, vol. 53, no. 20, p. 5595, 2008. [PubMed: 18799830]

[34]. Yveborg M, Danielsson M, and Bornefalk H, “Theoretical comparison of a dual energy system and photon counting silicon detector used for material quantification in spectral CT,” IEEE Trans. Med. Imag, vol. 34, no. 3, pp. 796–806, 3 2015.

[35]. Symons R, Krauss B, Sahbaee P, Cork TE, Lakshmanan MN, Bluemke DA et al., “Photon-counting CT for simultaneous imaging of multiple contrast agents in the abdomen: An in vivo study,” Med. Phys, vol. 44, no. 10, pp. 5120–5127, 2017. [PubMed: 28444761]

[36]. Cormode DP, Si-Mohamed S, Bar-Ness D, Sigovan M, Naha PC, Balegamire J et al., “Multicolor spectral photon-counting computed tomography: in vivo dual contrast imaging with a high count rate scanner,” Sci. Rep, vol. 7, no. 1, p. 4784, 2017. [PubMed: 28684756]

[37]. Symons R, Cork TE, Lakshmanan MN, Evers R, Davies-Venn C, Rice KA et al., “Dual-contrast agent photon-counting computed tomography of the heart: initial experience,” Int. J. Cardiovasc. Imaging, vol. 33, no. 8, pp. 1253–1261, 8 2017. [PubMed: 28289990]

[38]. Tao S, Rajendran K, McCollough CH, and Leng S, “Multi-contrast imaging on dual-source photon-counting-detector (PCD) CT,” in Medical Imaging 2019: Physics of Medical Imaging, vol. 10948 SPIE, 2019, pp. 1118–1124.

[39]. Fredette NR, Kavuri A, and Das M, “Multi-step material decomposition for spectral computed tomography,” Phys. Med. Biol, vol. 64, no. 14, p. 145001, 7 2019. [PubMed: 31216514]

[40]. Momose A, Kawamoto S, Koyama I, Hamaishi Y, Takai H, and Suzuki Y, “Demonstration of x-ray Talbot interferometry,” Jpn. J. Appl. Phys., Part 2, vol. 42, no. 7B, pp. 866–8, 2003.

[41]. Weitkamp T, Diaz A, David C, Pfeiffer F, Stampanoni M, Cloetens P et al., “X-ray phase imaging with a grating interferometer,” Opt. Exp, vol. 12, no. 16, pp. 6296–304, 2005.

[42]. Pfeiffer F, Weitkamp T, Bunk O, and David C, “Phase retrieval and differential phase-contrast imaging with low-brilliance x-ray sources,” Nat. Phys, vol. 2, no. 4, pp. 258–261, 4 2006.

[43]. Pfeiffer F, Bech M, Bunk O, Kraft P, Eikenberry EF, Brönnimann C et al., “Hard-x-ray dark-field imaging using a grating interferometer,” Nat. Mater, vol. 7, no. 2, pp. 134–137, 2 2008. [PubMed: 18204454]

[44]. Zambelli J, Bevins N, Qi Z, and Chen G-H, “Radiation dose efficiency comparison between differential phase contrast CT and conventional absorption CT,” Med. Phys, vol. 37, pp. 2473–2479, 2010. [PubMed: 20632558]

[45]. Qi Z, Zambelli J, Bevins N, and Chen G-H, “Quantitative imaging of electron density and effective atomic number using phase contrast CT,” Phys. Med. Biol, vol. 55, pp. 2669–2677, 2010. [PubMed: 20400806]

[46]. Chen G-H, Zambelli J, Li K, Bevins N, and Qi Z, “Scaling law for noise variance and spatial resolution in differential phase contrast computed tomography,” Med. Phys, vol. 38, pp. 584–588, 2011. [PubMed: 21452695]

[47]. Stampanoni M, Wang Z, Thüring T, David C, Roessl E, Trippel M et al., “The first analysis and clinical evaluation of native breast tissue using differential phase-contrast mammography.” Invet. Radiol, vol. 46, no. 12, pp. 801–6, 12 2011.

[48]. Stutman D, Beck TJ, Carrino J. a., and Bingham CO, “Talbot phase-contrast x-ray imaging for the small joints of the hand.” Phys. Med. Biol, vol. 56, no. 17, pp. 5697–720, 9 2011. [PubMed: 21841214]

[49]. Tapfer A, Bech M, Velroyen A, Meiser J, Mohr J, Walter M et al., “Experimental results from a preclinical X-ray phase-contrast CT scanner.” Proc. Natl. Acad. Sci. USA, vol. 109, no. 39, pp. 15 691–6, 9 2012.

[50]. Li K, Ge Y, Garrett J, Bevins N, Zambelli J, and Chen G-H, “Grating-based phase contrast tomosynthesis imaging: Proof-of-concept experimental studies,” Med. Phys., vol. 41, no. 1, 1 2014.

[51]. Garrett J, Ge Y, Li K, and Chen G-H, “Anatomical background noise power spectrum in differential phase contrast and dark field contrast mammograms,” Med. Phys, vol. 41, no. 12, p. 120701, 2014. [PubMed: 25471946]

[52]. Koehler T, Daerr H, Martens G, Kuhn N, Löscher S, van Stevendaal U et al., “Slit-scanning differential x-ray phase-contrast mammography: Proof-of-concept experimental studies,” Med. Phys, vol. 42, no. 4, pp. 1959–1965, 2015. [PubMed: 25832086]

[53]. Miao H, Gomella A. a., Harmon KJ, Bennett EE, Chedid N, Znati S et al., "Enhancing Tabletop X-Ray Phase Contrast Imaging with Nano-Fabrication," Sci. Rep, vol. 5, p. 13581, 2015. [PubMed: 26315891]

[54]. Birnbacher L, Willner M, Velroyen A, Marschner M, Hipp A, Meiser J et al., "Experimental realisation of high-sensitivity laboratory x-ray grating-based phase-contrast computed tomography," Sci. Rep, vol. 6, no. 10 2015, p. 24022, 2016. [PubMed: 27040492]

[55]. Li K, Zhang R, Garrett J, Ge Y, Ji X, and Chen G-H, "Design, construction, and initial results of a prototype multi-contrast x-ray breast imaging system," in Medical Imaging 2018: Physics of Medical Imaging, vol. 10573 SPIE, 2018, pp. 234–239.

[56]. Braig E, Bohm J, Dierolf M, Jud C, Gunther B, Mechlem K et al., "Direct quantitative material decomposition employing grating-based X-ray phase-contrast CT," Sci. Rep, vol. 8, no. 1, p. 16394, 2018. [PubMed: 30401876]

[57]. Feng M, Ji X, Treb K, Zhang R, Chen G-H, and Li K, "Spectrum optimization in photon counting detector based iodine K-edge CT imaging," in Medical Imaging 2019: Physics of Medical Imaging, vol. 10948 SPIE, 2019, pp. 324–329.

[58]. Brooks RA, "A quantitative theory of the hounsfield unit and its application to dual energy scanning," J. Comput. Assist. Tomo, vol. 1, no. 4, pp. 487–493, 1977.

[59]. Strobl M, "General solution for quantitative dark-field contrast imaging with grating interferometers," Sci. Rep, vol. 4, pp. 1–6, 2014.

[60]. Mechlem K, Sellerer T, Viermetz M, Herzen J, and Pfeiffer F, "Spectral differential phase contrast x-ray radiography," IEEE Trans. Med. Imag, pp. 1–1, 2019.

[61]. Jensen TH, Bech M, Zanette I, Weitkamp T, David C, Deyhle H et al., "Directional x-ray dark-field imaging of strongly ordered systems," Phys. Rev. B, vol. 82, no. 21, p. 214103, 2010.

[62]. Malecki A, Potdevin G, Biernath T, Eggl E, Willer K, Lasser T et al., "X-ray tensor tomography," EPL (Europhysics Letters), vol. 105, no. 3, p. 38002, 2 2014.

[63]. Tang X, Yang Y, and Tang S, "Characterization of imaging performance in differential phase contrast CT compared with the conventional CT-noise power spectrum NPS(k)," Med. Phys, vol. 38, pp. 4386–4395, 2011. [PubMed: 21859039]

[64]. Li K, Bevins N, Zambelli J, and Chen G, "Fundamental relationship between the noise properties of grating-based differential phase contrast CT and absorption CT: Theoretical framework using a cascaded system model and experimental validation," Med. Phys, vol. 40, no. 2, p. 021908, 2013. [PubMed: 23387756]

[65]. Krauss B, Grant KL, Schmidt BT, and Flohr TG, "The importance of spectral separation: An assessment of dual-energy spectral separation for quantitative ability and dose efficiency," Invest. Radiol, vol. 50, no. 2, pp. 114–118, 2015. [PubMed: 25373305]

[66]. NIST, "XCOM: Photon Cross Sections Database." [Online]. Available: (https://physics.nist.gov/PhysRefData/Xcom/html/xcom1.html)

[67]. Ji X, Ge Y, Zhang R, Li K, and Chen G-H, "Studies of signal estimation bias in grating-based x-ray multicontrast imaging," Med. Phys, vol. 44, no. 6, pp. 2453–2465, 2017. [PubMed: 28339107]

[68]. Maaß C, Baer M, and Kachelrieß M, "Image-based dual energy CT using optimized precorrection functions: A practical new approach of material decomposition in image domain," Med. Phys, vol. 36, no. 8, pp. 3818–3829, 2009. [PubMed: 19746815]

[69]. Willner M, Bech M, Herzen J, Zanette I, Hahn D, Kenntner J et al., "Quantitative x-ray phase-contrast computed tomography at 82 kev," Opt. Express, vol. 21, no. 4, pp. 4155–4166, 2 2013. [PubMed: 23481949]

[70]. Thüring T, Abis M, Wang Z, David C, and Stampanoni M, "X-ray phase-contrast imaging at 100 keV on a conventional source," Sci. Rep, vol. 4, no. 1, p. 5198, 2014. [PubMed: 24903579]

[71]. Hauke C, Horn F, Pelzer G, Rieger J, Lachner S, Ludwig V et al., "Construction and evaluation of a high-energy grating-based x-ray phase-contrast imaging setup," in Medical Imaging 2016: Physics of Medical Imaging, vol. 9783, International Society for Optics and Photonics. SPIE, 2016, pp. 1445–1451.

[72]. Gromann LB, De Marco F, Willer K, Noël PB, Scherer K, Renger B et al., "In-vivo x-ray dark-field chest radiography of a pig," Sci. Rep, vol. 7, no. 1, pp. 1–7, 2017. [PubMed: 28127051]

[73]. Raupach R and Flohr TG, “Analytical evaluation of the signal and noise propagation in x-ray differential phase-contrast computed tomography,” Phys. Med. Biol, vol. 56, no. 7, pp. 2219–2244, 2011. [PubMed: 21403187]

[74]. Köhler T, Engel KJ, and Roessl E, “Noise properties of grating-based x-ray phase contrast computed tomography,” Med. Phys, vol. 38, pp. S106–S116, 2011. [PubMed: 21978111]

[75]. Wang AS and Pelc NJ, “Optimal energy thresholds and weights for separating materials using photon counting x-ray detectors with energy discriminating capabilities,” in Medical Imaging 2009: Physics of Medical Imaging, vol. 7258 SPIE, 2009, pp. 664–675.

[76]. Zheng Y, Yveborg M, Grnberg F, Xu C, Su Q, Danielsson M et al., “Robustness of optimal energy thresholds in photon-counting spectral CT,” Nucl. Instrum. Meth. A, vol. 953, p. 163132, 2020.

[77]. Brendel B, Von Teuffenbach M, Noël PB, Pfeiffer F, and Koehler T, “Penalized maximum likelihood reconstruction for x-ray differential phase-contrast tomography,” Med. Phys, vol. 43, no. 1, pp. 188–194, 2016. [PubMed: 26745911]

[78]. Long Y and Fessler JA, “Multi-material decomposition using statistical image reconstruction for spectral CT,” IEEE Trans. Med. Imag, vol. 33, no. 8, pp. 1614–1626, 8 2014.

[79]. Lee S, Choi Y-N, and Kim H-J, “Quantitative material decomposition using spectral computed tomography with an energy-resolved photon-counting detector,” Phys. Med. Biol, vol. 59, no. 18, pp. 5457–5482, 8 2014. [PubMed: 25164993]

[80]. Yu Z, Leng S, Li Z, and McCollough CH, “Spectral prior image constrained compressed sensing (spectral PICCS) for photon-counting computed tomography,” Phys. Med. Biol, vol. 61, no. 18, pp. 6707–6732, 8 2016. [PubMed: 27551878]

[81]. Lu Y, Geret J, Unberath M, Manhart M, Ren Q, Fahrig R et al., “Projection-based material decomposition by machine learning using image-based features for computed tomography,” in The 13th International Meeting on Fully Three-Dimensional Image Reconstruction in Radiology and Nuclear Medicine, 2015, pp. 448–452.

[82]. Zhang W, Zhang H, Wang L, Wang X, Hu X, Cai A et al., “Image domain dual material decomposition for dual-energy CT using butterfly network,” Med. Phys, vol. 46, no. 5, pp. 2037–2051, 2019. [PubMed: 30883808]

[83]. Li Z, Ravishankar S, Long Y, and Fessler JA, “DECT-MULTRA: Dual-energy CT image decomposition with learned mixed material models and efficient clustering,” 2019, arXiv:1901.00106.

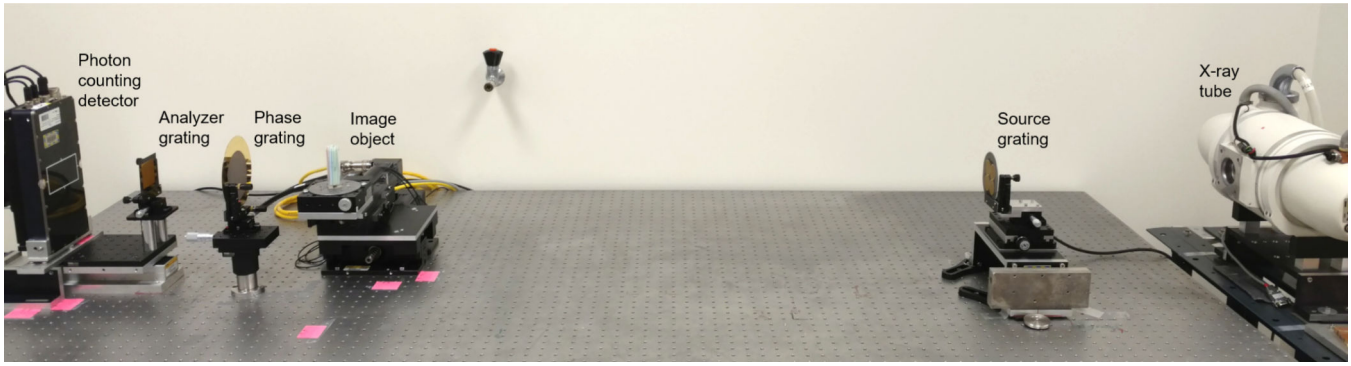

Fig. 1.

A photo of the constructed DE-DPC-CT system where a three-grating interferometer is incorporated into a photon counting CT imaging system with two energy bins.

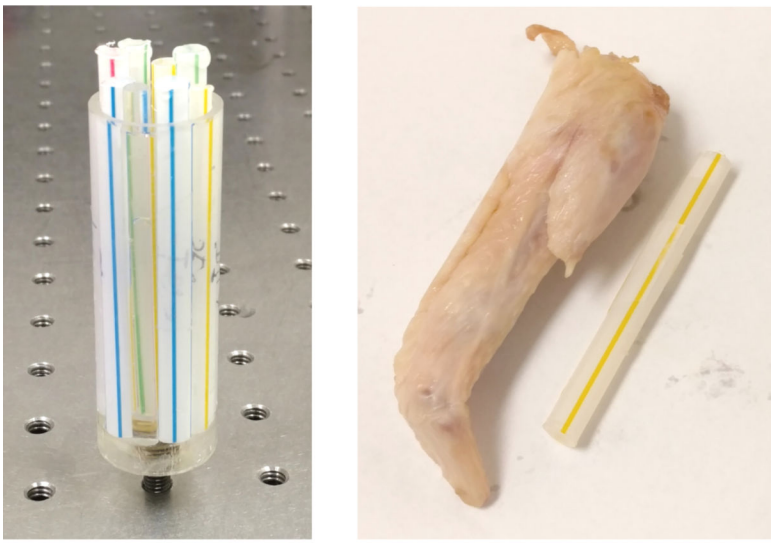

Fig. 2.
(a) Inserts of solutions placed in a water-filled PMMA container. (b) The Formalin-fixed Chicken wing and a solution insert with 32 mg/mL iodine.

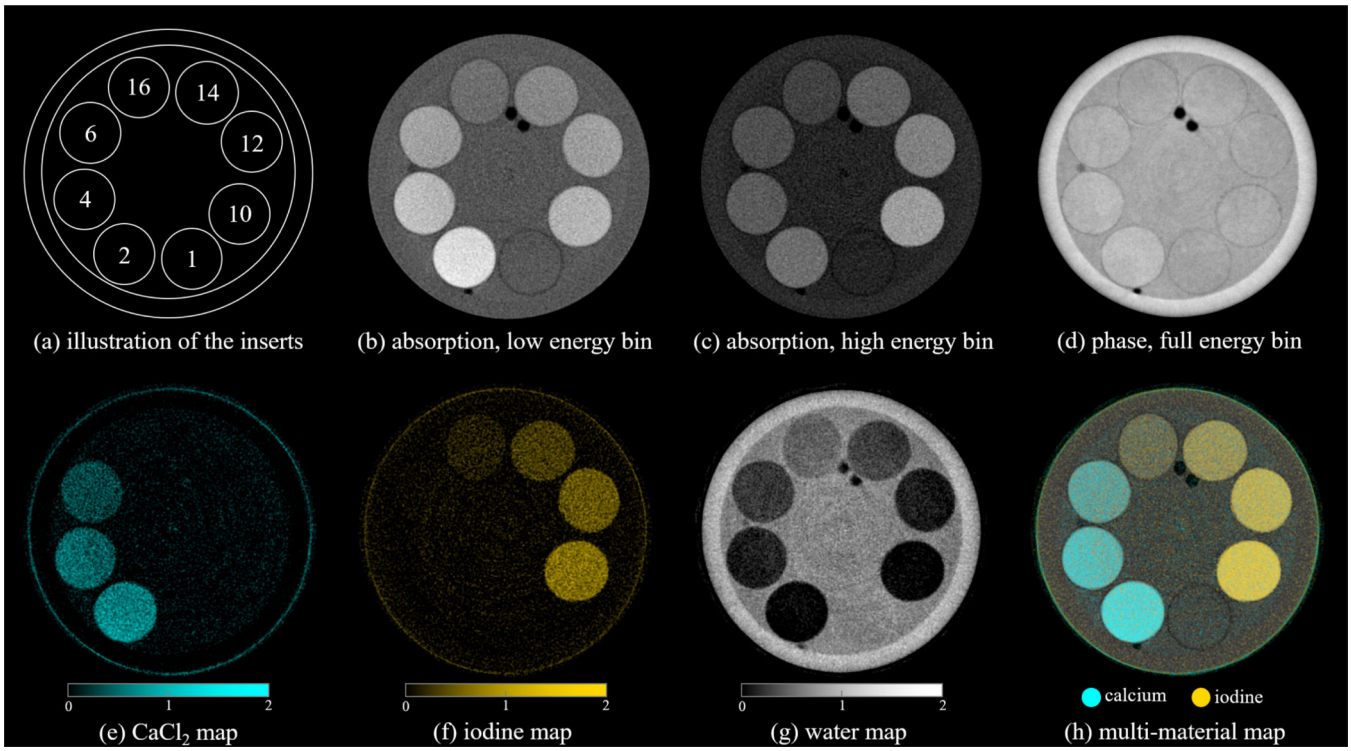

Fig. 3.

Images of insert group #1 from the DE-DPC-CT scan. (a) illustration of the material and concentration of the inserts. The meaning of the indices are listed in Table II. (b)-(d) Reconstructed absorption and phase images from different energy bins. The black spots are the air bubbles in water. Display range: (b)-(c): **[0.2, 0.6]** cm^{-1}; (d): **[0.14, 0.32]** × $\mathbf{10^{-6}}$. (e)-(g) Decomposition coefficient maps. The color bars are indicated below the images. (h) Multi-material map made by overlaying the calcium map and iodine map onto the full bin absorption image.

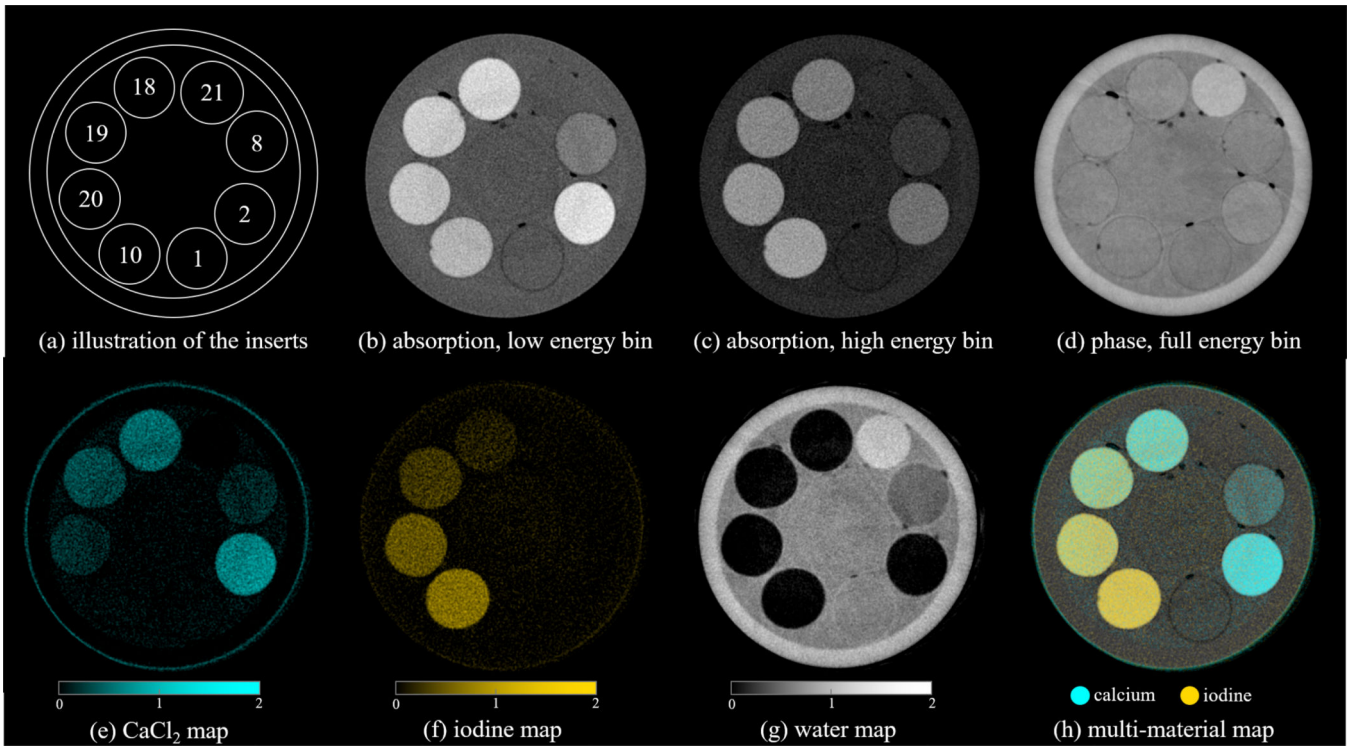

Fig. 4.

Images of insert group #2 from the DE-DPC-CT scan. The descriptions of the sub-figures are similar to those of Figure 3.

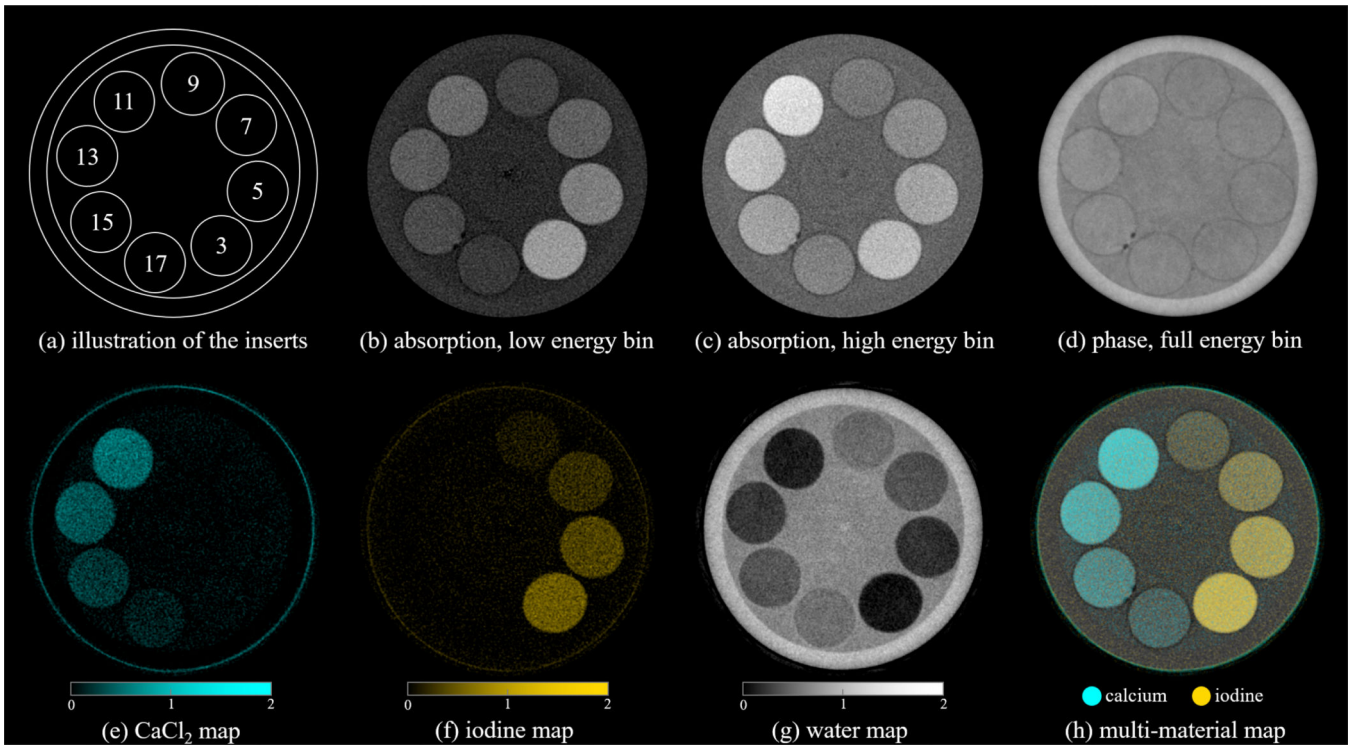

Fig. 5.

Images of insert group #3 from the DE-DPC-CT scan. The descriptions of the sub-figures are similar to those of Figure 3.

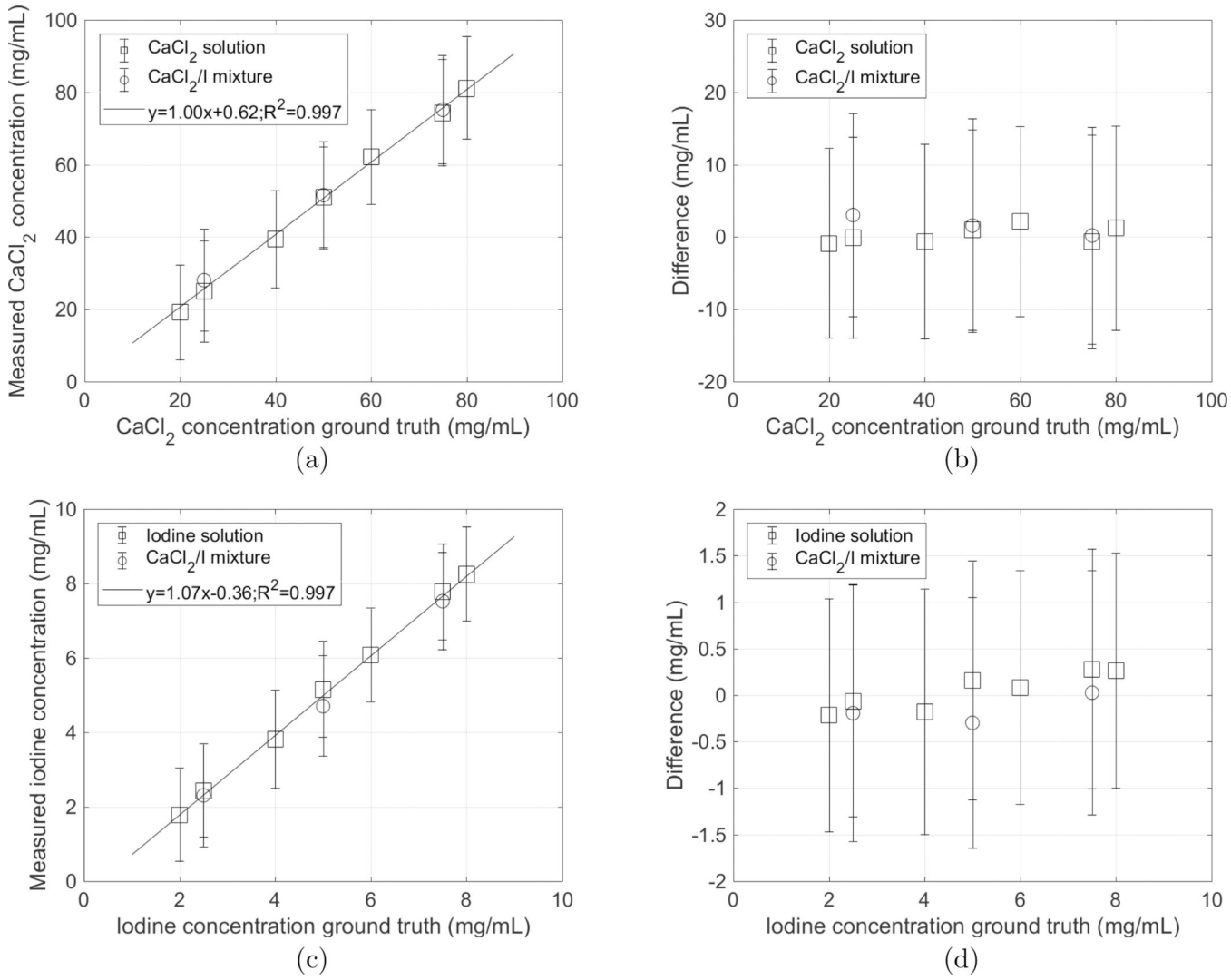

Fig. 6.

Comparison of the measured concentrations and the ground truth concentrations for $CaCl_2$ and iodine. The square data points represent the concentrations when the solution is a $CaCl_2$-only or iodine-only solution. The circlar data points represent the concentrations for the $CaCl_2$-iodine mixtures. (a) and (c) are plots of the measured concentrations vs the ground truths for $CaCl_2$ and iodine, respectively. (b) and (d) are plots of differences between the measured concentrations and the ground truths versus the ground truths for $CaCl_2$ and iodine, respectively.

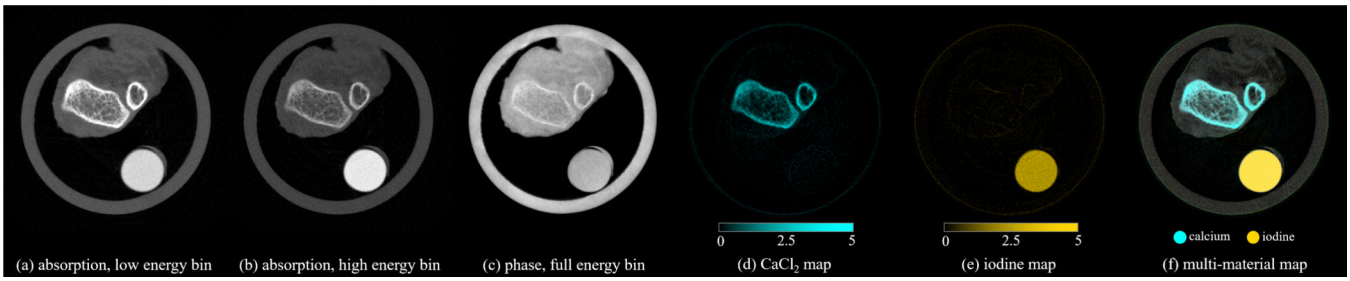

Fig. 7.

(a)-(c) Reconstructed abortion and phase images from different energy bins. Display range: (a)-(b): **[0,1.0]** cm^{-1}; (c): **[0.05, 0.32] ×10^{-6}**. (d)-(e) Decomposition coefficient map. The color bars are indicated below the images. (f) multi-material map by overlaying the calcium map and iodine map onto the full energy bin absorption image

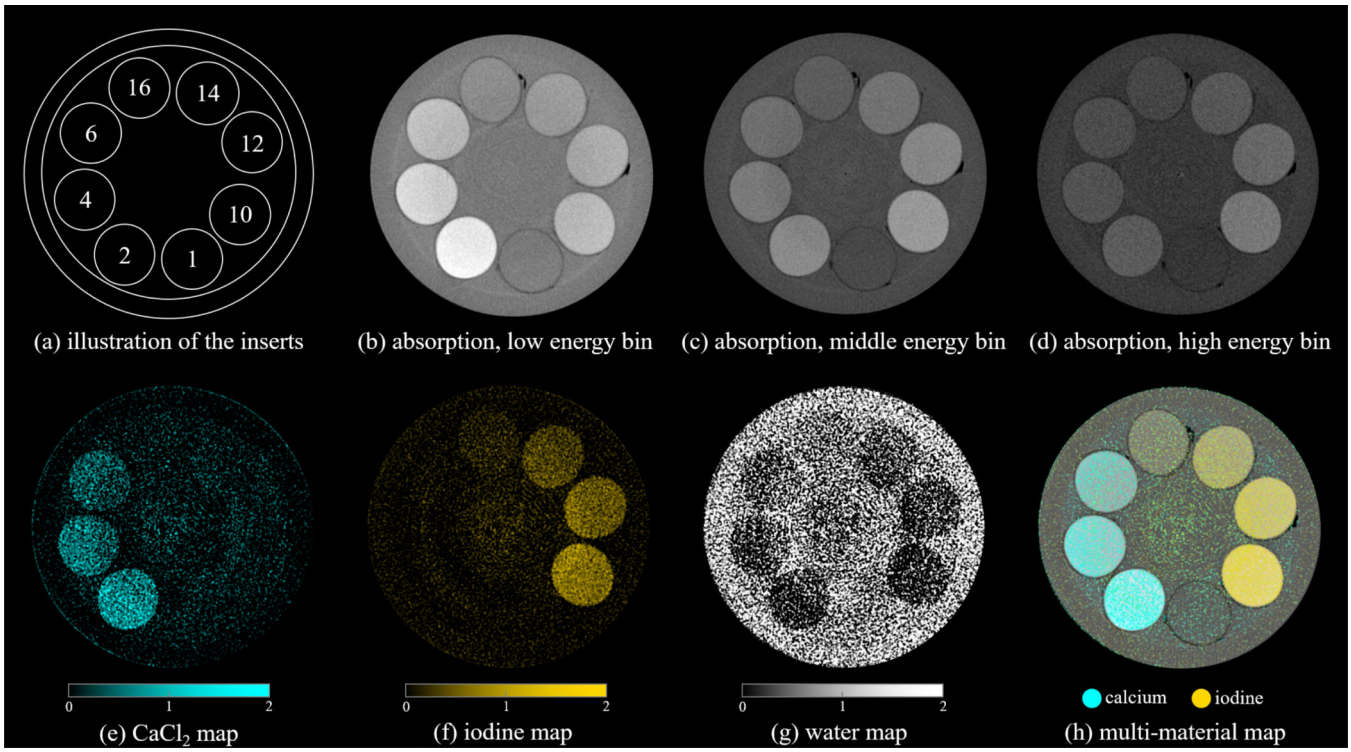

Fig. 8.

Images of insert group #1 from the triple spectra scan. (a) illustration of the material and concentration of the inserts. The meaning of the indices are listed in Table II. (b)-(d) Reconstructed absorption and phase images from different energy bins. Display range: [**0.1, 0.7**] cm^{-1}. (e)-(g) Decomposition coefficient map. The color bars are indicated below the images. (h) Multi-material map made by overlaying the calcium map and iodine map onto the full bin absorption image.

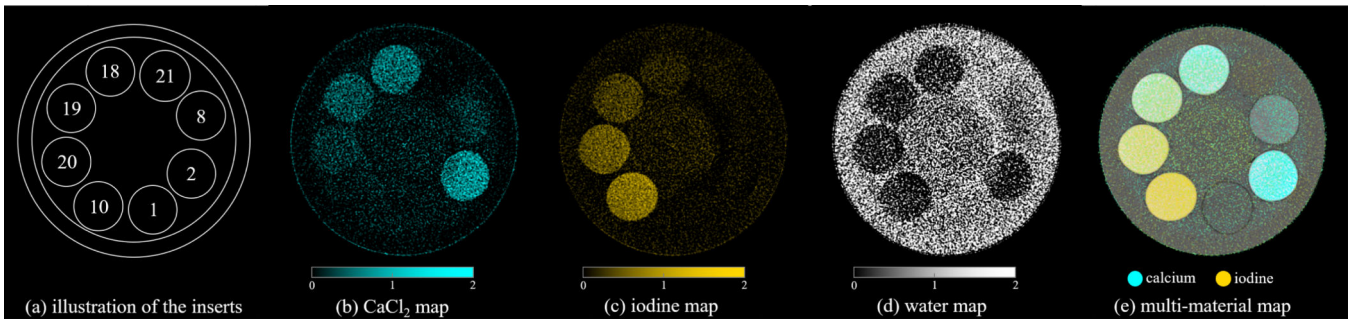

Fig. 9.

Images of insert group #2 from the triple spectra scan. (a) illustration of the material and concentration of the inserts. (b)-(d) Decomposition coefficient map. The color bars are indicated below the images. (e) Multi-material map made by overlaying the calcium map and iodine map onto the full bin absorption image.

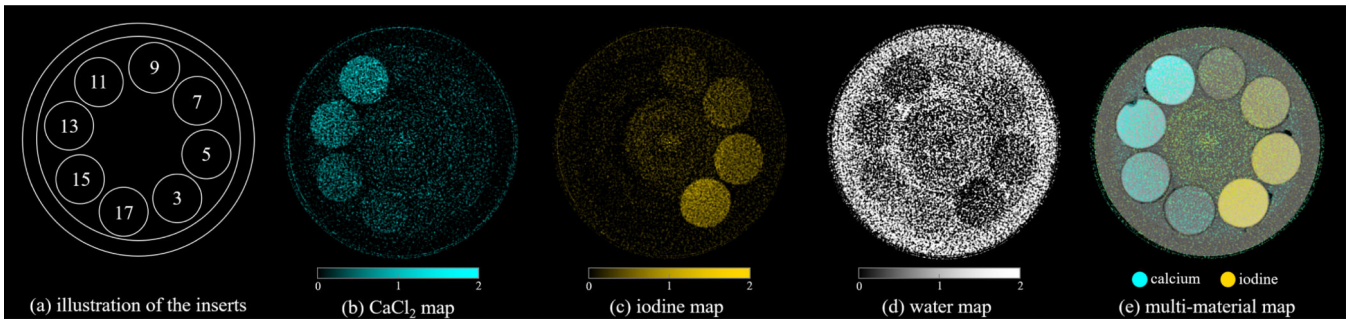

Fig. 10.

Images of insert group #3 from the triple spectra scan.. The descriptions of the sub-figures are similar to those of Figure 9.

TABLE I

PARAMETERS OF THE GRATINGS

	Pitch size (μm)	**Duty cycle**	**Grating type**
G0	20.7	35%	absorption grating
G1	4.3	50%	π-phase grating
G2	2.4	50%	absorption grating

TABLE II

LIST OF THE MATERIALS AND CONCENTRATIONS. CONCENTRATIONS ARE INDICATED IN THE PARENTHESIS (UNIT: MG/ML).

Index	Material (concentration)	Index	Material and concentration
1	water	12	iodine (7.5)
2	$CaCl_2$ (100)	13	iodine (6)
3	$CaCl_2$ (80)	14	iodine (5)
4	$CaCl_2$ (75)	15	iodine (4)
5	$CaCl_2$ (60)	16	iodine (2.5)
6	$CaCl_2$ (50)	17	iodine (2)
7	$CaCl_2$ (40)	18	$CaCl_2$ (75) iodine (2.5)
8	$CaCl_2$ (25)	19	$CaCl_2$ (50) iodine (5)
9	$CaCl_2$ (20)	20	$CaCl_2$ (25) iodine (7.5)
10	Iodine (10)	21	PMMA
11	Iodine (8)		

TABLE III

SUMMARY OF THE DECOMPOSITION COEFFICIENTS (MEAN±STD) FROM THE DE-DPC-CT SCAN FOR THE INSERTS. THE VALUES IN THE PARENTHESIS INDICATE THE GROUND TRUTH.

#	$CaCl_2$ basis	Iodine basis	water basis
3	0.81 ± 0.14 (0.8)	−0.03 ± 0.13 (0)	0.22 ± 0.08 (0.2)
4	0.74 ± 0.15 (0.75)	−0.00 ± 0.13 (0)	0.26 ± 0.09 (0.25)
5	0.62 ± 0.13 (0.6)	−0.03 ± 0.13 (0)	0.42 ± 0.08 (0.4)
6	0.51 ± 0.14 (0.5)	0.05 ± 0.13 (0)	0.44 ± 0.08 (0.5)
7	0.39 ± 0.13 (0.4)	−0.03 ± 0.13 (0)	0.66 ± 0.08 (0.6)
8	0.25 ± 0.14 (0.25)	−0.02 ± 0.13 (0)	0.79 ± 0.08 (0.75)
9	0.19 ± 0.13 (0.2)	−0.03 ± 0.12 (0)	0.86 ± 0.07 (0.8)
11	0.04 ± 0.13 (0)	0.83 ± 0.13 (0.8)	0.14 ± 0.08 (0.2)
12	0.02 ± 0.14 (0)	0.78 ± 0.13 (0.75)	0.18 ± 0.08 (0.25)
13	0.03 ± 0.14 (0)	0.61 ± 0.13 (0.6)	0.36 ± 0.08 (0.4)
14	0.01 ± 0.14 (0)	0.52 ± 0.13 (0.5)	0.48 ± 0.09 (0.5)
15	0.01 ± 0.13 (0)	0.38 ± 0.13 (0.4)	0.63 ± 0.08 (0.6)
16	0.01 ± 0.14 (0)	0.24 ± 0.12 (0.25)	0.74 ± 0.09 (0.75)
17	0.01 ± 0.14 (0)	0.18 ± 0.13 (0.2)	0.82 ± 0.08 (0.8)
18	0.75 ± 0.15 (0.75)	0.23 ± 0.14 (0.25)	0.03 ± 0.09 (0)
19	0.52 ± 0.15 (0.5)	0.47 ± 0.14 (0.5)	0.03 ± 0.08 (0)
20	0.28 ± 0.14 (0.25)	0.75 ± 0.13 (0.75)	−0.04 ± 0.10 (0)
21	−0.32 ± 0.14 (−0.38)	0.01 ± 0.13 (0)	1.49 ± 0.08 (1.60)

TABLE IV

SUMMARY OF THE DECOMPOSITION COEFFICIENTS (MEAN±STD) FROM THE TRIPLE SPECTRA SCAN FOR THE INSERTS. THE VALUES IN THE BRACKET INDICATE THE GROUND TRUTH.

#	$CaCl_2$ basis	Iodine basis	water basis
3	0.80 ± 0.40 (0.8)	−0.05 ± 0.24 (0)	0.28 ± 0.96 (0.2)
4	0.75 ± 0.44 (0.75)	−0.01 ± 0.25 (0)	0.27 ± 1.05 (0.25)
5	0.61 ± 0.41 (0.6)	−0.05 ± 0.23 (0)	0.48 ± 0.97 (0.4)
6	0.50 ± 0.44 (0.5)	0.03 ± 0.24 (0)	0.50 ± 1.04 (0.5)
7	0.39 ± 0.38 (0.4)	−0.04 ± 0.23 (0)	0.68 ± 0.93 (0.6)
8	0.22 ± 0.37 (0.25)	−0.02 ± 0.23 (0)	0.84 ± 0.91 (0.75)
9	0.19 ± 0.38 (0.2)	−0.03± 0.23 (0)	0.87 ± 0.94 (0.8)
11	0.01 ± 0.42 (0)	0.83 ± 0.25 (0.8)	0.15 ± 1.02 (0.2)
12	0.02 ± 0.43 (0)	0.79 ± 0.25 (0.75)	0.17 ± 1.04 (0.25)
13	0.00 ± 0.39 (0)	0.61 ± 0.23 (0.6)	0.39 ± 0.95 (0.4)
14	0.02 ± 0.42 (0)	0.55 ± 0.24 (0.5)	0.40 ± 1.02 (0.5)
15	0.02 ± 0.40 (0)	0.41 ± 0.24 (0.4)	0.54 ± 0.97 (0.6)
16	−0.02 ± 0.42 (0)	0.23 ± 0.24 (0.25)	0.82 ± 1.01 (0.75)
17	0.01 ± 0.40 (0)	0.19 ± 0.25 (0.2)	0.80 ± 0.99 (0.8)
18	0.74 ± 0.38 (0.75)	0.24 ± 0.24 (0.25)	0.04 ± 0.95 (0)
19	0.53 ± 0.36 (0.5)	0.51 ± 0.23 (0.5)	−0.06 ± 0.89 (0)
20	0.26 ± 0.38 (0.25)	0.75 ± 0.24 (0.75)	0.00 ± 0.95 (0)
21	−0.24 ± 0.34 (−0.38)	0.10 ± 0.21 (0)	1.22 ± 0.85 (1.60)